PNAS
www.pnas.org

Supplementary Information for

Label-free visualization and characterization of extracellular vesicles in breast cancer

Sixian You, Ronit Barkalifa, Eric J. Chaney, Haohua Tu, Jaena Park, Janet Elise Sorrells, Yi Sun, Yuan-Zhi Liu, Lin Yang, Danny Z. Chen, Marina Marjanovic, Saurabh Sinha, Stephen A. Boppart

Corresponding author: Stephen A. Boppart
Email: boppart@illinois.edu

This PDF file includes:

Supplementary text
Figures S1 to S9
Legends for Movies S1 to S9
References for SI reference citations

Other supplementary materials for this manuscript include the following:

Movies S1 to S9

www.pnas.org/cgi/doi/10.1073/pnas.1909243116

Supplementary Information Text

Supplementary Materials and Methods

Human breast tissue. Fresh samples of human breast tissue were obtained from Carle Foundation Hospital and imaged within 6 hours after surgery. Tissue was stored in a cold saline solution at 2-8 °C before imaging. Normal breast tissue samples (7 subjects, 52 imaging sites) were obtained from female subjects undergoing breast reduction surgery with no history of cancer. Cancerous breast tissue samples were obtained from female subjects undergoing mastectomy or lumpectomy procedures (12 subjects, 53 imaging sites) and diagnosed by a board-certified pathologist as having invasive ductal carcinoma.

Animal studies. To induce mammary tumors in the female Wistar-Furth rats (Harlan, IN), NMU (N-Nitroso-N-methylurea) (MilliporeSigma, St. Louis, MO) diluted in distilled water (12.5 mg/mL) was injected intraperitoneally at a concentration of 55 mg/kg into the left side of the abdomen when the animals were 7 weeks old [1, 2]. One week later, the same amount of NMU was injected intraperitoneally into the right side of the abdomen. After approximately 12 weeks of age (5 weeks post injection), when mammary tumors became palpable, the rat was prepared for *in vivo* imaging. Rats were anesthetized with 1% isoflurane mixed with O_2, at a flow rate of 1 L/min for surgery and imaging sessions. Surgery was performed to reflect back overlying skin and expose the primary tumor and its neighboring mammary tissue while the rat was under isoflurane anesthesia. During the imaging sessions, physiological temperature was maintained by a heating blanket. Imaging duration was kept under 3 hours to avoid complications of long-term anesthesia. Rats (total of 5 tumor-bearing and 5 control rats) were euthanized immediately after imaging.

EV isolation from cells. The following human cell lines were used: MCF10A (human mammary epithelial cells, ATCC), MCF-7 (ER-positive, PR-positive and HER2-negative human adenocarcinoma cells, ATCC), and MDA-MB-231 (triple-negative human metastatic breast carcinoma cells, ATCC). Cells were grown in T75 cm^2 flasks in complete cell media according to supplier-recommended protocols until they reached a confluency of 70% to 80%. Cells were subsequently washed three times with serum-free media and incubated with serum-free media for 24 hours. EVs were isolated from cell culture media by differential centrifugation as described in previous work with some modifications [3]. In brief, the conditioned media was collected and centrifuged at 800 g for 10 min, followed by a centrifugation step of 2,000 g for 30 min to remove cellular debris. The supernatant was then centrifuged at 10,000 g for 1 h at 4 ºC to obtain the 10K pellet. Afterwards, the supernatant was further centrifuged at 100,000 g for 1 h at 4 ºC to obtain the 100K pellet. All the pellets were washed with 30 ml PBS and centrifuged again at 10,000 g for 1 h (same for 100,000 g). The final 10K pellet and 100K pellet were each re-suspended in 100 µl of PBS for imaging later. The rotor type used in this study was a SureSpin 630 (36 ml, Thermo Scientific). More details can be found in the submission of experimental parameters to the EV-TRACK knowledgebase via the following URL: http://evtrack.org/review.php with the EV-TRACK ID (EV180074).

Optical setup of the label-free multiphoton microscope. The light emission from an industrial fiber laser (Satsuma, Amplitude Systemes) operated at 10 MHz was guided into a photonic crystal fiber (PM-LMA-15, NKT Photonics) to generate the high-power (1.8 W) coherent supercontinuum needed for multiphoton imaging [4]. The generated supercontinuum was then sent into a 640-pixel 4-f pulse shaper (MIIPS Box640, BioPhotonic Solutions Inc.) to select and pulse-shape the 1110 ± 30 nm band of the supercontinuum for subsequent excitation. The 1110 ± 30 nm pulses from the pulse shaper were delivered via raster scanning by a galvanometer-driven mirror pair (6215H, Cambridge Technology) and focused by a multiphoton objective (XLPLN25XWMP2 25X, N.A.=1.05, Olympus), with an average power of 14 mW incident on the sample after the loss along the excitation beam path. The reflected multimodal multiphoton signals were then spectrally-separated into 4 detection channels by long-pass

dichroic mirrors and bandpass filters (Semrock, Inc.) and detected by 4 photon-counting photomultiplier tubes (H7421-40, Hamamatsu).

Specifically, the THG channel was detected using a band-pass 365-375 nm filter, 3PF by 420-480 nm, SHG by 540-570 nm, and 2PF by 580-640 nm. Assignment of channels was consistent with previous publications [4–6]. Minimization of crosstalk between FAD and NADH detection despite simultaneous excitation was demonstrated previously. The power dependence of these two channels was further validated here using FAD (F6625, MilliporeSigma, St. Louis, MO, USA) and NADH (N8129, MilliporeSigma, St. Louis, MO, USA) solutions of 1 mM (SI Appendix, Fig. S2), with intensities detected from NADH matching cubic power dependence and FAD following quadratic dependence, as expected.

Despite this unconventional excitation scheme, we showed that fluorescence detected in the 420-480 nm band was dominated by NAD(P)H emission, as indicated by fluorescence intensity changes induced by mitochondrial inhibitor NaCN (1 mM), which is similar to the observation made with 750-nm excitation [7]. The effect of the same treatment on FAD appeared much less significant, which echoes the concern that the 2PF channel alone might not be entirely specific to FAD. Within biological tissue, there are multiple endogenous fluorophores with similar spectral characteristics. Among them, lipofuscins and porphyrins are the most prominent auto-fluorophores in the spectral window of 600-650 nm [8]. Lipofuscin is a brown-yellow pigment that accumulates with age in the lysosomes of post-mitotic cells, and has been associated with the retinal pigment epithelium, neurons, and cardiac myocytes [9]. Porphyrins and their derivatives were observed to be present in abundance in red blood cells as well as in sebaceous plugs associated with human hair follicles [8, 10]. Considering all these factors (2PF signal intensity, cell morphology, and context), FAD is the most probable source of autofluorescence when detected in the cell cytoplasm within the context of the mammary tumor microenvironment. To compare the performance of this setting for FAD against more conventional setups (excitation at 900 nm), we generated images from the same sites using two separate spectral bands (900 nm vs 1110 nm) using the same supercontinuum. As expected, the conventional 900-nm excitation yielded a higher intensity than our 1110-nm excitation as the excitation wavelength is tuned away from the optimal excitation peak. However, the image content did not suffer dramatic information loss or distortion from visual inspection (SI Appendix, Fig. S3). In addition, the signal-to-noise ratio was not significantly compromised, considering the lower background when using 1110-nm excitation. For these reasons, and for simplicity, the 2PF channel was assigned to FAD in this work considering the combination of the 2PF signal intensity, the cellular morphology, and the context of the microenvironment.

Specimens or samples to be imaged (living animal, fresh human tissue, live cell culture, or isolated EVs) were placed on a three-dimensional piezoelectric stage to enable mosaic-mode imaging and volumetric imaging, with the imaging plane placed 20-200 μm below the tissue surface. Pixel dwelling time ranged from 4-20 μs depending on the temporal and spatial resolution required for the application, typically resulting in a 2-10 second acquisition time for each 400 x 400 μm^2 (800 x 800 pixel) image. Full details can be found in previous studies [4, 11].

Transmission electron microscopy (TEM). For ultrastructural analysis of isolated EVs, electron microscopy was performed using a transmission electron microscope (Phillips CM200, FEI Company). Uranyl acetate (2%) was used to negatively stain the vesicles in the samples.

Nanoparticle tracking analysis. Nanoparticle tracking analysis (measurement of the concentration and size of the EVs) was performed by using a commercial Nanosight system (NS300, NanoSight) on EV samples diluted in PBS. A constant flow pump was used and three videos of 30-second duration were recorded for each dataset.

Image processing and analysis. Images were processed and analyzed as described in previous work [4]. In each frame, the four channels (THG, 3PF, SHG, 2PF) were acquired

simultaneously and saved as individual four-channel images. For mosaic acquisition, tiles were stitched together using a custom-written MATLAB (Mathworks, Natick, Mass) script that matched sub-image boundaries based on the predicted position map of each tile. For volumetric imaging and real-time imaging, the tiles were stacked and displayed as a four-channel video. Without any further preprocessing, the four-channel image/video was loaded into FIJI (National Institutes of Health) to apply pseudo-color maps to merge the contrast. The same color maps were used consistently throughout the study, namely magenta for THG, cyan for 3PF, green for SHG, and yellow for 2PF, with colors assigned based on the closest wavelength emissions of the label-free multiphoton signals being emitted from the specimens and samples.

EVs were first segmented from the multimodal images based on their optical signature and morphology using U-Net [12]. Training data was provided by manual labeling of individual EVs and corresponding raw 4-channel multiphoton images with subsequent data augmentation (flip, rotation, contrast randomization). The segmentation step was performed in Tensorflow 1.12.0. After semantic segmentation, intensities of each EV were extracted together with their spatial location. The AUC values from using the abundance of NAD(P)H-rich EVs to identify different breast cancer stages were determined by logistic regression based on features of interest (e.g. concentration and percentage of NAD(P)H-rich EVs). All statistical analysis was performed in MATLAB.

Statistical analysis. Statistical significance was assessed using a two-tailed Student's t-test and one-way ANOVA. Results with $p<0.05$ were considered statistically significant. For comparisons of multiple groups, Tukey's post hoc test was used after a significant ANOVA test to further determine the significant differences between groups. The histograms of EV optical signatures were modeled via a bimodal Gaussian distribution, with two vertical dashed lines indicating the means of the two modes. In each box plot, the central line was the median value of the distribution, and the top and bottom limits of the box indicated upper and lower quantiles, respectively. The whiskers extend to the most extreme data points not considered outliers, and the outliers were plotted individually using the '+' symbol (MATLAB).

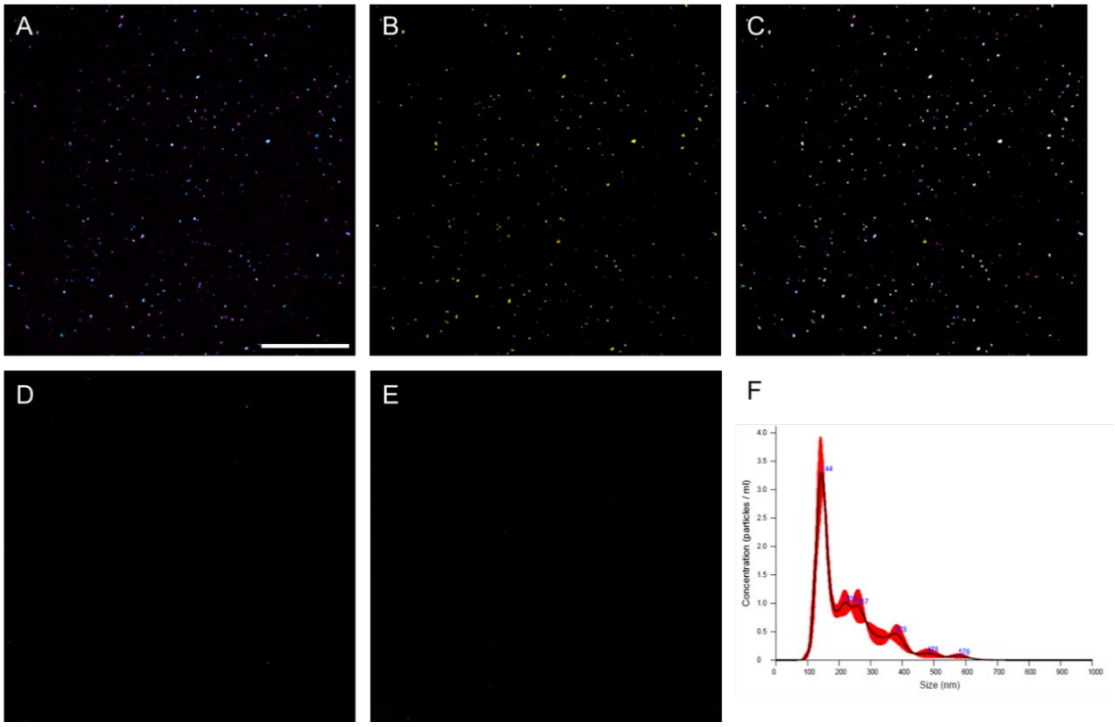

Fig. S1. Multiphoton composite images for stained EVs, stained negative control, and unstained negative control samples, and EV size distribution measured by NTA.
(A) Overlay of the label-free multiphoton imaging channels (magenta channel assigned to THG and cyan to 3PF of NAD(P)H) from the PKH26-stained EV samples. (B) PKH26 (membrane dye) channel of the same stained EV sample as shown in (A). (C) Overlay of the label-free channels and the labeled channel from the same stained EV sample. (D) Composite image of PKH26-treated control sample (isolated from media without cells). (E) Composite image of label-free control sample. (F) Size measurement of EVs by NTA. Scale bar: 50 μm.

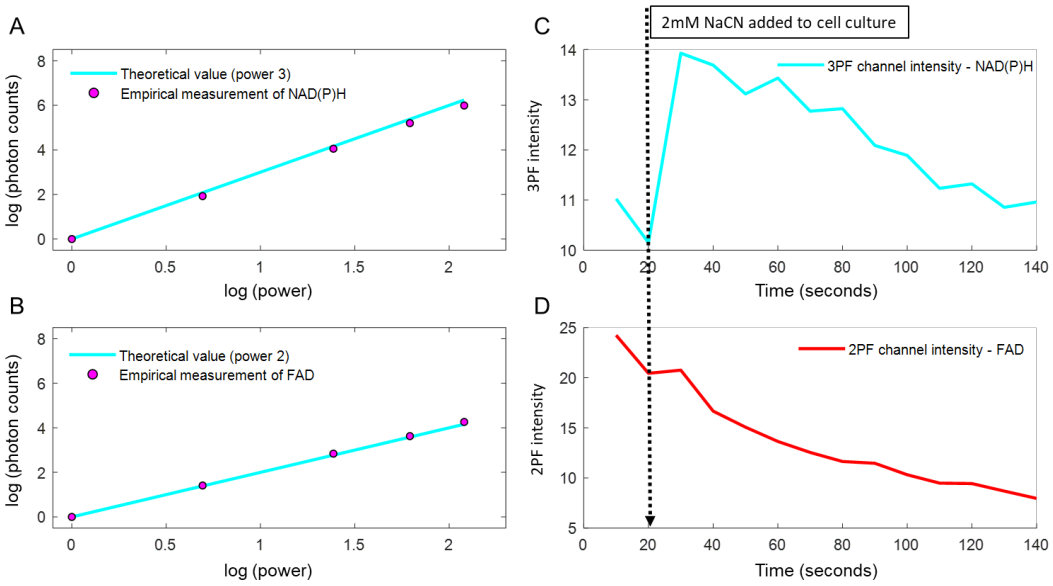

Fig. S2. Validation of power dependence and sensitivity of using NADH and FAD solution. **(**A) Signal dependence on power of NAD(P)H solution and (B) FAD solution. (C) Fluorescence intensity changes induced by mitochondrial inhibitor NaCN (1 mM) in the NAD(P)H channel and (D) FAD channel.

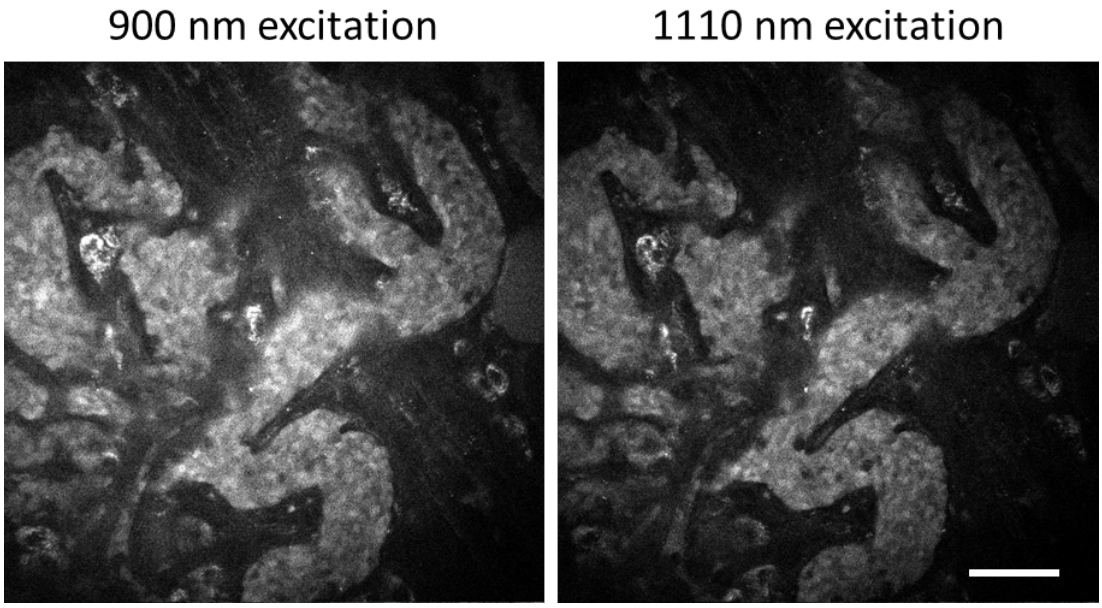

Fig. S3. Comparison of FAD signal excited by 900 nm excitation and 1110 nm excitation. Scale bar: 50 μm.

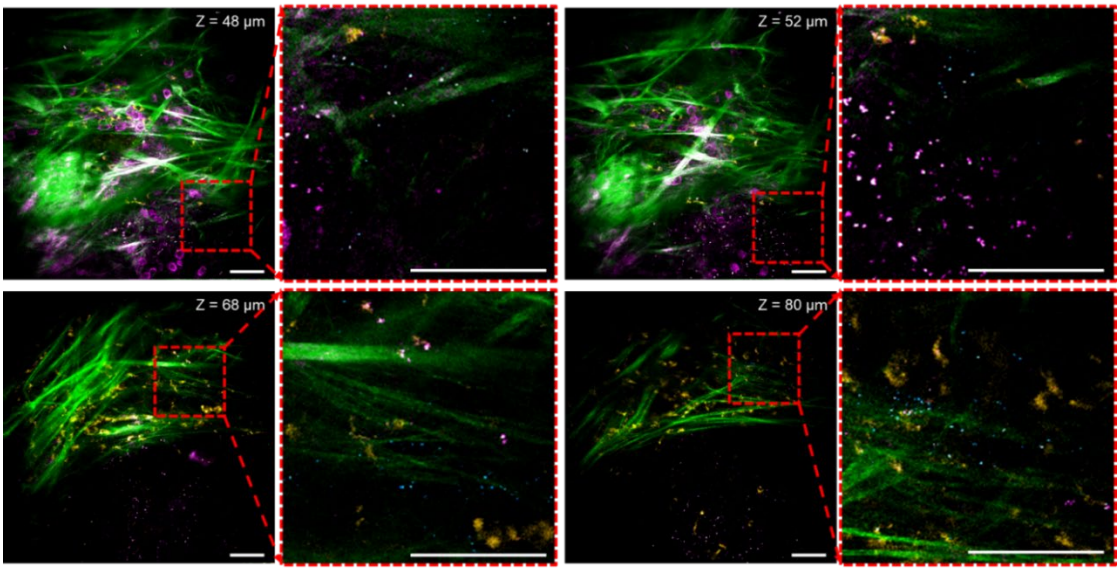

Fig. S4. Representative images of EVs at different depths of the tumor site. Images highlight the volumetric distribution of NAD(P)H-rich (cyan) and THG-high (magenta) vesicles at the tumor site (Fig. 2A and Movie S1). Scale bar: 50 µm.

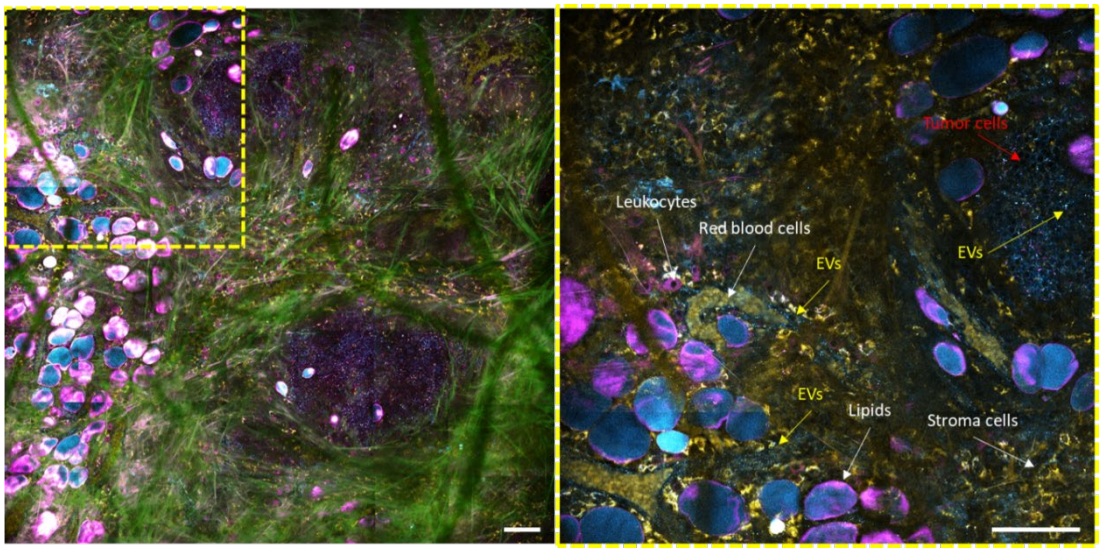

Fig. S5. *In vivo* imaging of tumor microenvironment highlighting the presence of NAD(P)H-rich EVs scattered around within and near the tumor region. Yellow box on the left panel indicates the region that is zoomed in on the right panel. Scale bar: 100 μm.

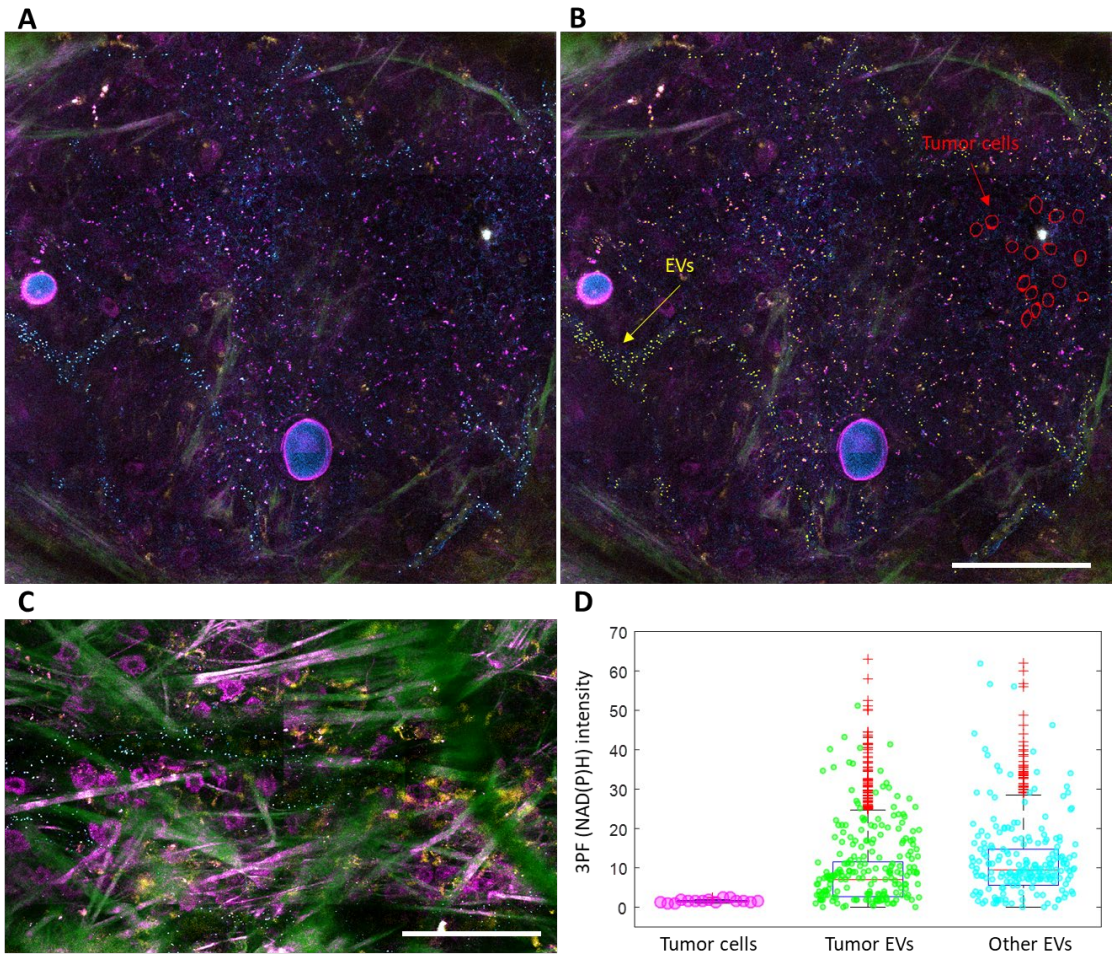

Fig. S6. EVs carry >5-times higher concentration of NAD(P)H than neighboring tumor cells. (A,B) Zoomed-in image of the red dashed box from Fig. 2A, with tumor cells and the neighboring tumor EVs highlighted by red circles and yellow dots, respectively in (B). (C) Zoomed-in image of the white dashed box from Fig. 2A, highlighting EVs that are surrounded by non-NAD(P)H-rich microenvironmental components, such as collagen fibers (green, SHG), stromal cells (yellow, 2PF), and leukocytes (magenta, THG) [4]. (D) 3PF (NAD(P)H) intensity of tumor cells, tumor EVs, and EVs that are not in the proximity of tumor cells or NAD(P)H-rich cells. The mean values (average concentration of NAD(P)H within each measured unit) of these three groups (1.60 vs. 8.77 vs. 11.25) are significantly different from each other based on statistical tests (ANOVA, post-hoc Tukey-Kramer test, $p<0.0001$). Scale bar: 100 μm.

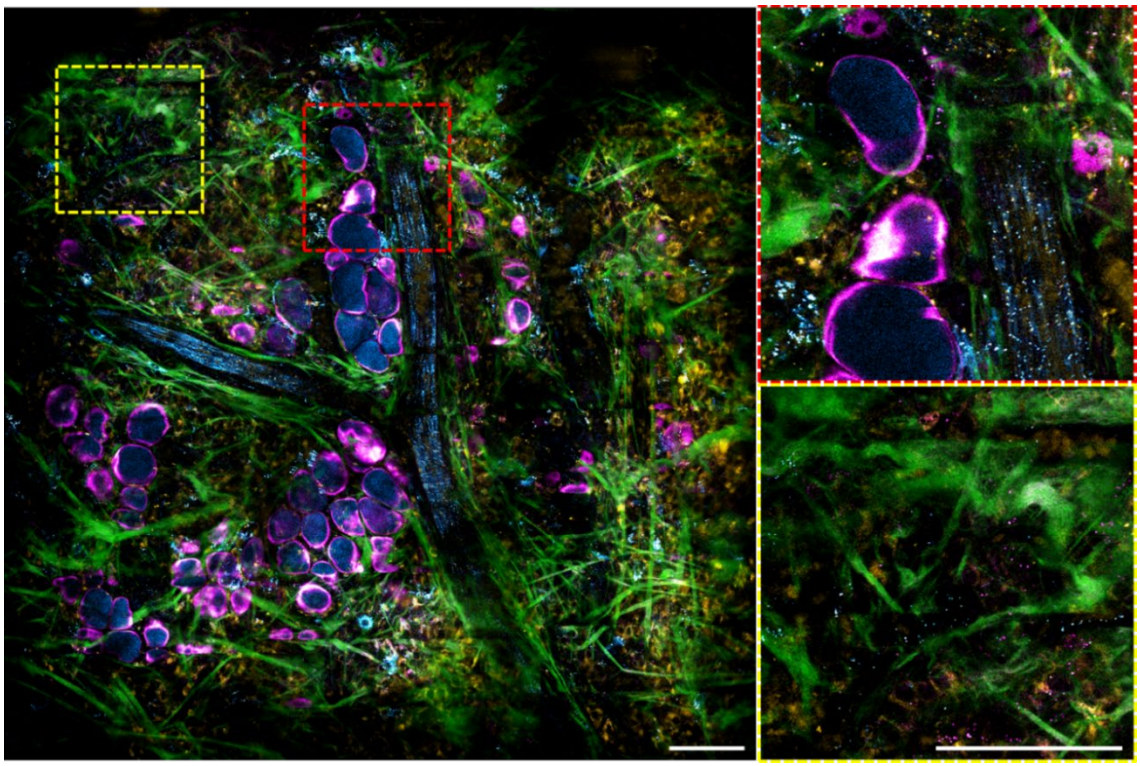

Fig. S7. *In vivo* imaging of tumor microenvironment highlighting the presence of NAD(P)H-rich EVs scattered outside tumor region (yellow dashed box) and along the blood vessels (red dashed box). Corresponding volumetric data can be found in Movie S2. Scale bar: 100 μm.

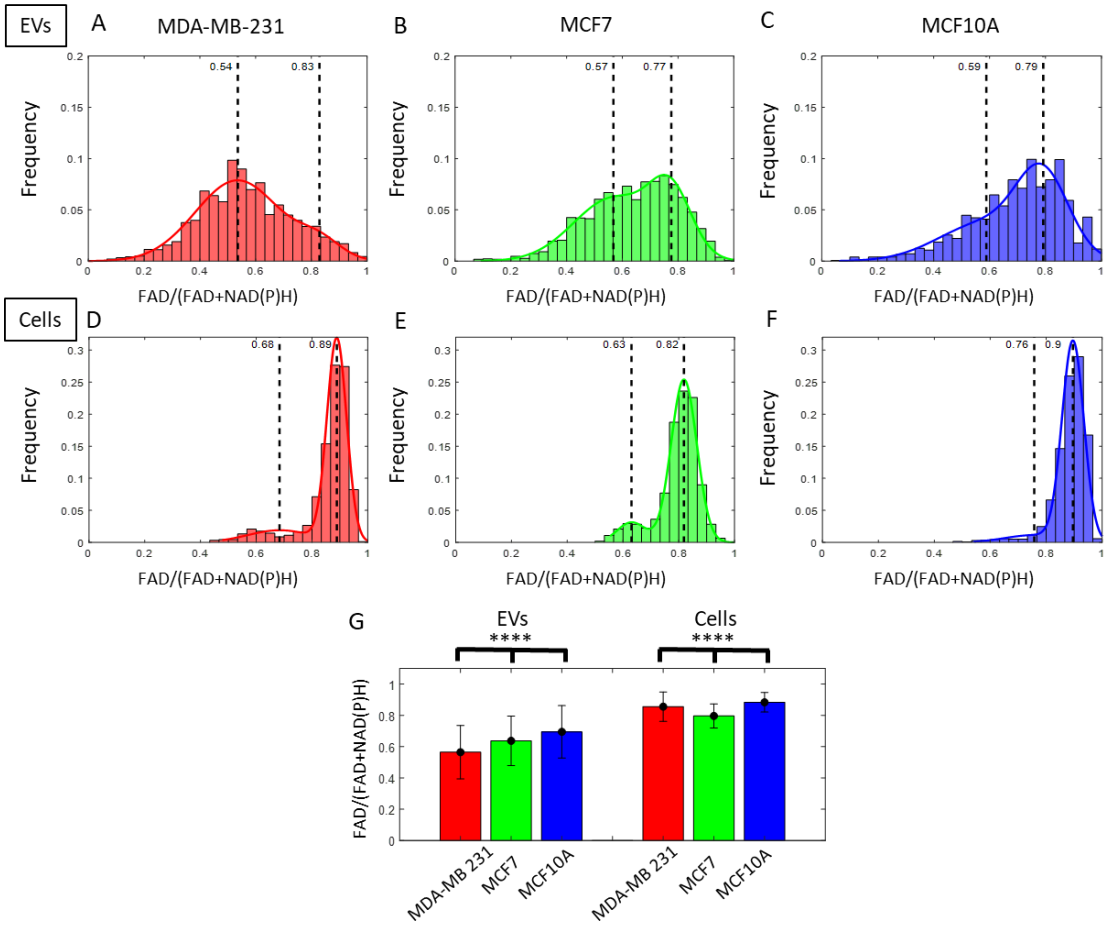

Fig. S8. Correlation between the optical signatures of EVs and parent cells.
(A-C) Histograms of the FAD/(FAD+NAD(P)H) values of EVs isolated from different breast cell lines. The histograms of EV optical signatures are modeled via a bimodal Gaussian distribution, with two vertical dashed lines indicating the means of the two modes. (D-F) Histograms of the FAD/(FAD+NAD(P)H) values of parent cells from which the EVs from (A-C) were isolated. The cells were plated in an imaging dish and characterized *in vitro*. (G) Comparison of the average NAD(P)H levels in EVs versus the parent cells (**** p<0.0001 by ANOVA, post-hoc Tukey-Kramer test. Error bars represent standard deviation). As a result of HER2 activation, MCF7 cells potentially upregulate glycolysis and produce significantly more NAD(P)H and lower redox ratio compared to HER2-absent MCF10A and MDA-MB-231 cells. This modulation effect of NAD(P)H was not observed in EVs.

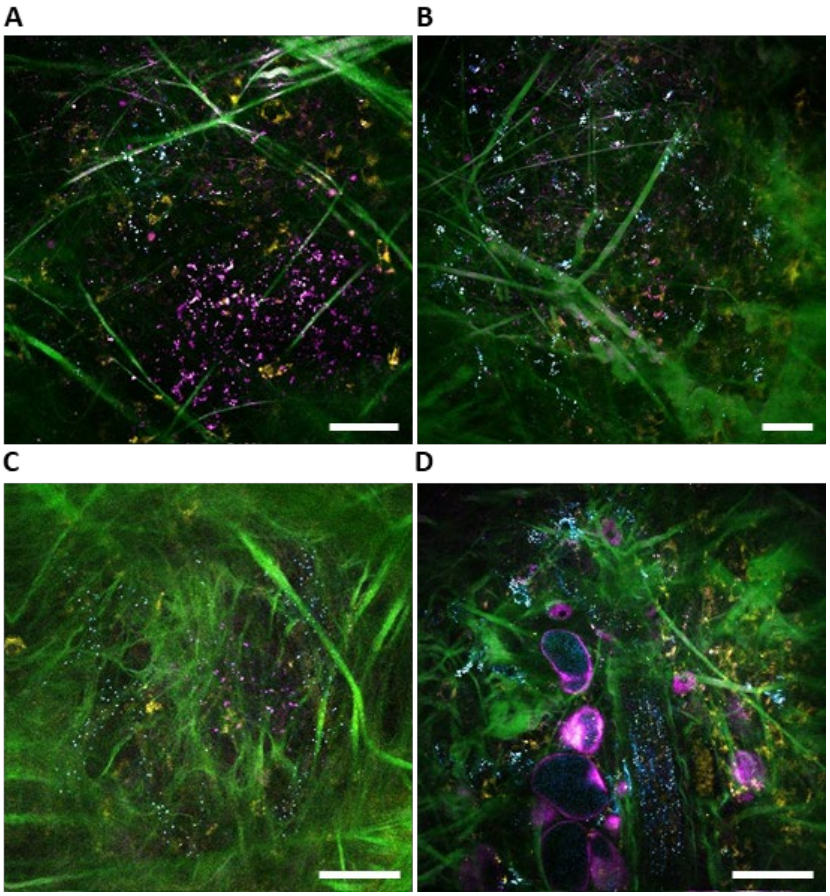

Fig. S9. Representative images of time-lapse videos (Movie S6-9) showing relatively stationary EVs at tumor sites of rat mammary cancer *in vivo*. (A) Recording of THG-high (magenta) EVs within the tumor (Movie S6). (B) Recording of a mix of THG-high and NAD(P)H-high EVs within the tumor (Movie S7). (C) Recording of a mix of THG-high and NAD(P)H-high EVs at the blood vessel walls near the tumor (Movie S8). (D) Recording of NAD(P)H-high (cyan) EVs at periphery of the blood vessel walls in the living tumor microenvironment (Movie S9). Scale bar: 50 μm.

Legends for movie S1-9

Movie S1: Volumetric image stack from 48 μm to 80 μm below the surface. Data correspond to Fig. 2A and SI Appendix, Fig. S4. Similar to the figures, the same color maps were used consistently for all the videos. Magenta represents THG signals (optical heterogeneity), which highlights the lipid-water interface such as membranes and lipid droplets. Cyan represents 3PF signals, which is correlation with NAD(P)H concentration. Green represents SHG signals (optical non-centrosymmetry), which highlight Type-I collagen fibers. Yellow represents 2PF signals, which is correlated with FAD concentration.

Movie S2: 3D imaging from 40 μm to 120 μm below the surface. Data correspond to Fig. S7.

Movie S3: Release of a vesicle in live MDA-MB-231 cell culture. Data correspond to Fig. 4A.

Movie S4: Migration of a vesicle via a cell protrusion in live MDA-MB-231 cell culture. Data correspond to Fig. 4B.

Movie S5: Uptake of a vesicle in live MDA-MB-231 cell culture. Data correspond to Fig. 4C.

Movie S6: Time-lapse videos showing relatively stationary THG-high (magenta) EVs within the tumor in living rat mammary cancer. Data correspond to SI Appendix, Fig. S9A.

Movie S7: Time-lapse videos showing relatively stationary EVs (a mix of THG-high and NAD(P)H-high EVs) within the tumor in living rat mammary cancer. Data correspond to SI Appendix, Fig. S9B.

Movie S8: Time-lapse videos showing relatively stationary EVs (mix of THG-high and NAD(P)H-high) at the blood vessel walls near tumor in living rat mammary cancer. Data correspond to SI Appendix, Fig. S9C.

Movie S9: Time-lapse videos showing relatively stationary NAD(P)H-high (cyan) EVs at periphery of the blood vessel walls in the living tumor microenvironment. Data correspond to SI Appendix, Fig. S9D.

References

1. Gullino PM, Pettigrew HM, Grantham FH (1975) N-nitrosomethylurea as mammary gland carcinogen in rats. J Natl Cancer Inst 54:401–414.

2. Cha RS, Thilly WG, Zarbl H (2006) N-nitroso-N-methylurea-induced rat mammary tumors arise from cells with preexisting oncogenic Hras1 gene mutations. Proc Natl Acad Sci 91:3749–3753. https://doi.org/10.1073/pnas.91.9.3749

3. Clancy JW, Sedgwick A, Rosse C, et al (2015) Regulated delivery of molecular cargo to invasive tumour-derived microvesicles. Nat Commun 6:6919. https://doi.org/10.1038/ncomms7919

4. You S, Tu H, Chaney EJ, et al (2018) Intravital imaging by simultaneous label-free autofluorescence-multiharmonic microscopy. Nat Commun 9:2125. https://doi.org/10.1038/s41467-018-04470-8

5. You S, Sun Y, Chaney EJ, et al (2018) Slide-free virtual histochemistry (Part I): development via nonlinear optics. Biomed Opt Express 9:5240-5252. https://doi.org/10.1364/boe.9.005240

6. You S, Sun Y, Chaney EJ, et al (2018) Slide-free virtual histochemistry (Part II): detection of field cancerization. Biomed Opt Express 9:5253-5268. https://doi.org/10.1364/boe.9.005253

7. Huang S, Heikal AA, Webb WW (2002) Two-photon fluorescence spectroscopy and microscopy of NAD(P)H and flavoprotein. Biophys J 82:2811–2825. https://doi.org/10.1016/S0006-3495(02)75621-X

8. Croce AC, Bottiroli G (2014) Autofluorescence spectroscopy and imaging: a tool for biomedical research and diagnosis. Eur J Histochem 58:2461. https://doi.org/10.4081/ejh.2014.2461

9. Terman A, Brunk UT (1998) Lipofuscin: mechanisms of formation and increase with age. APMIS 106:265–276. https://doi.org/10.1111/j.1699-0463.1998.tb01346.x

10. Chen Q, Hirsch RE (2006) A direct and simultaneous detection of zinc protoporphyrin IX, free protoporphyrin IX, and fluorescent heme degradation product in red blood cell hemolysates. Free Radic Res 40:285-294. https://doi.org/10.1080/10715760500522630

11. Tu H, Liu Y, Turchinovich D, et al (2016) Stain-free histopathology by programmable supercontinuum pulses. Nat Photonics 10:534–540. https://doi.org/10.1038/nphoton.2016.94

12. Ronneberger O, Fischer P, Brox T (2015) U-Net: convolutional networks for biomedical image segmentation. MICCAI (Springer, Cham, Switzerland), pp 234–241.